Uniformly rotating, axisymmetric, and triaxial quark stars in general relativity

Enping Zhou,[1,2] Antonios Tsokaros,[2,3] Luciano Rezzolla,[2,4] Renxin Xu,[1,5] and Kōji Uryū[6]

[1]*State Key Laboratory of Nuclear Science and Technology and School of Physics, Peking University, Beijing 100871, People's Republic of China*

[2]*Institute for Theoretical Physics, Frankfurt am Main 60438, Germany*

[3]*Department of Physics, University of Illinois at Urbana-Champaign, Urbana, Illinois 61801, USA*

[4]*Frankfurt Institute of Advanced Studies, Frankfurt am Main 60438, Germany*

[5]*Kavli Institute for Astronomy and Astrophysics, Peking University, Beijing, 100871, People's Republic of China*

[6]*Department of Physics, University of the Ryukyus, Senbaru, Nishihara, Okinawa 903-0213, Japan*

(Received 31 October 2017; published 19 January 2018)

Quasiequilibrium models of uniformly rotating axisymmetric and triaxial quark stars are computed in a general-relativistic gravity scenario. The Isenberg-Wilson-Mathews (IWM) formulation is employed and the Compact Object Calculator (COCAL) code is extended to treat rotating stars with finite surface density and new equations of state (EOSs). Besides the MIT bag model for quark matter which is composed of deconfined quarks, we examine a new EOS proposed by Lai and Xu that is based on quark clustering and results in a stiff EOS that can support masses up to 3.3 $M_\odot$ in the case we considered. We perform convergence tests for our new code to evaluate the effect of finite surface density in the accuracy of our solutions and construct sequences of solutions for both small and high compactness. The onset of secular instability due to viscous dissipation is identified and possible implications are discussed. An estimate of the gravitational wave amplitude and luminosity based on quadrupole formulas is presented and comparison with neutron stars is discussed.

DOI: 10.1103/PhysRevD.97.023013

I. INTRODUCTION

The recent gravitational-wave (GW) event GW170817, together with accompanying electromagnetic emission observations [1,2] from a binary neutron star (BNS) merger, has opened a brand new multimessenger observation era for us to explore the Universe. Apart from enriching our knowledge on origins of short gamma-ray bursts [3] and nucleosynthesis associated with BNS mergers [4,5], it also provides an effective way for us to constrain the equation of state (EOS) of neutron stars (NSs). In addition to systems such as binary black-hole mergers and BNS mergers, rapidly rotating compact stars have also been considered as important candidates of GW sources [6], which could be detected by ground-based GW observatories [7–11] and help us understand the nature of strong interaction of dense matter.

It has been a long time since the equilibrium models of self-gravitating, uniformly rotating, incompressible fluid stars were systematically studied in a Newtonian gravity scheme [12]. Depending on the rotational kinetic energy, the configuration could be axisymmetric Maclaurin ellipsoids as well as nonaxisymmetric ellipsoids, such as Jacobian (triaxial) ellipsoids. For compact stars that we are interested in for GW astronomy, however, general relativity is required to replace Newtonian gravity. The field of relativistic rotating stars has been studied for many years [13,14].

A rotating NS will spontaneously break its axial symmetry if the rotational kinetic energy to gravitational binding energy ratio, $T/|W|$, exceeds a critical value. This instability can either be of secular type [15–18] or dynamical [19–27], depending on the process driving the instability and with only small modifications if a magnetization is present [28–30] (see [31] for a review). A high $T/|W|$ ratio can also be reached for a newly born rotating compact star during a core collapse supernova or for a NS which is spun up by accretion [32–36].

Quasiequilibrium figures of triaxially rotating NSs have also been created and studied in full general relativity [37,38]. In this case, the bifurcation from an axisymmetric to triaxial configuration happens very close to the mass-shedding limit, and, for soft NS EOSs or for NSs with large compactness, the triaxial sequence could totally vanish [16,18,39–41]. As a result, it is presently unclear whether triaxial configurations of NSs can actually be realized in practice.

On the other hand, it is worth noting that the EOS of compact stars is still a matter of lively debate since astronomical observations are not sufficient to rule out

 © 2018 American Physical Society

many of the nuclear-physics EOSs that are compatible with the observations. As a result, besides the popular idea of NSs, other models for compact stars are possible and have been considered in the past. A particularly well-developed literature is the one concerned with strange quark stars (QSs), since it was long conjectured that strange quark matter composed of deconfined up, down, and strange quarks could be absolutely stable [42,43]. There is also possible observational evidence indicating the existence of QSs (for a recent example, see [44]). Additionally, the small tidal deformability of QSs is favored by the observation of GW170817 [45] and possible models with QS merger or QS formations have also been suggested to explain the electromagnetic counterparts for a short gamma-ray burst (cf. [45,46]).

Following this possibility, a large effort has been developed to calculate equilibrium configurations of QSs, starting from the first attempts [47–49]. At present, both uniformly rotating [50–52] and differentially rotating QSs [53] have been studied in full general relativity. Unlike NSs, which are bound by self-gravity, QSs are self-bound by strong interaction. Consequently, rotating QSs can reach a much larger $T/|W|$ ratio compared with NSs and the triaxial instability could play a more important role [50,54,55]. The triaxial bar mode (Jacobi-like) instability for the MIT bag-model EOS has been investigated in a general-relativistic framework [56].

We here use the Compact Object CALculator code, COCAL, to build general-relativistic triaxial QS solution sequences using different EOS models. COCAL is a code to calculate general-relativistic equilibrium and quasiequilibrium solutions for binary compact stars (black hole and NS) as well as rotating (uniformly or differentially) NSs [37,38,57–60]. The part of the COCAL code handling the calculation of the EOSs was originally designed for piecewise polytropic EOSs. We have here extended the code to include the polynomial type of EOSs, as those that can be used to describe QSs. In doing so, the trivial relationship between the thermodynamic quantities for a piecewise polytrope [e.g., see Eqs. (64)–(68) in [60]] is lost and now one has to apply root-finding methods. Another issue is related to the surface fitted coordinates that are used in COCAL to track the surface of the star. For NSs, the surface was identified as the place where the rest-mass density goes to zero or where the specific enthalpy becomes 1. This is no longer generally true for a self-bound QS and a different approach needs to be developed. The nonlinear algebraic system that determines the angular velocity, the constant from the Euler equation, and the renormalization constant of the spherical grid has to be modified in order to accommodate the arbitrary surface enthalpy.

We here compute solutions for both axisymmetric and triaxial rotating QSs with the new code, as well as sequences with various QS EOSs and different compactnesses. We checked our new implementation for those cases where previous studies have been possible [37], and we confirm the accuracy of our new code. We discuss the astrophysical implications of the quantities of rotating QSs at the bifurcation point. For instance, the spin frequency at the bifurcation point could be a more realistic spin-up limit for compact stars rather than the mass-shedding limit, which relates to the fastest spinning pulsar we might be able to observe. The GW strain and luminosity estimates for our models are given, while full numerical simulations are left for the future (see [61] for recent simulations involving triaxial NSs).

The structure of this paper is organized as follows. In Sec. II we discuss the formulation we used and the field equations (Sec. II A), the hydrodynamics (Sec. II B), and the EOS part (Sec. II C). In order to test the behavior of the modified code, we have performed convergence tests with five resolutions and compared with rotating NS solutions built by the original COCAL code. These tests can be found in Sec. III. Triaxially deformed rotating QS sequences for different compactnesses are presented in Sec. IV, while the implications for the astrophysical observations of this work are presented in Sec. VI. Hereafter, we use units with $G = c = M_\odot = 1$ unless otherwise stated; a conversion table to the standard cgs units can be found, for instance, in [62].

II. FORMULATION AND NUMERICAL METHOD

A. Field equations

In order to solve the field equations numerically, the Isenberg-Wilson-Mathews (IWM) formulation [63–65] is employed. In a coordinate chart $\{t, x^i\}$, the $3+1$ decomposition of the spacetime metric gives

$$ds^2 = -\alpha^2 dt^2 + \psi^4 \delta_{ij}(dx^i + \beta^i dt)(dx^j + \beta^j dt), \quad (1)$$

where α, β^i are the lapse and shift vector (the kinematical quantities), while $\gamma_{ij} = \psi^4 \delta_{ij}$ is the IWM approximation for the three-metric.

The extrinsic curvature of the foliation is defined by

$$K_{ab} := -\frac{1}{2\alpha}\partial_t \gamma_{ab} + \frac{1}{2\alpha}\pounds_\beta \gamma_{ab}, \quad (2)$$

and a maximal slicing condition $K = 0$ is assumed.

Decomposing the Einstein equations with respect to the normal n^α of foliation, we get the following five equations in terms of the five metric coefficients $\{\psi, \beta^a, \alpha\}$ on the initial slice Σ_0:

$$(G_{\alpha\beta} - 8\pi T_{\alpha\beta}) n^\alpha n^\beta = 0, \quad (3)$$

$$(G_{\alpha\beta} - 8\pi T_{\alpha\beta}) \gamma^{i\alpha} n^\beta = 0, \quad (4)$$

$$(G_{\alpha\beta} - 8\pi T_{\alpha\beta}) \left(\gamma^{\alpha\beta} + \frac{1}{2} n^\alpha n^\beta\right) = 0, \quad (5)$$

where the first and second equations are the Hamiltonian and momentum constraints, respectively. Here $\gamma_{\alpha\beta} = g_{\alpha\beta} + n_\alpha n_\beta$ is the projection tensor onto the spatial slices. These equations can be written in the form of elliptic equations with the nonlinear source terms, respectively,

$$\nabla^2\psi = -\frac{\psi^5}{8}A_{ab}A^{ab} - 2\pi\psi^5\rho_{\rm H}, \tag{6}$$

$$\nabla^2\beta^a + \frac{1}{3}\partial^a\partial_b\beta^b = -2\alpha A^{ab}\partial_b \ln\frac{\psi^6}{\alpha} + 16\pi\alpha j^a, \tag{7}$$

$$\nabla^2(\alpha\psi) = \frac{7}{8}\alpha\psi^5 A_{ab}A^{ab} + 2\pi\alpha\psi^5(\rho_{\rm H} + 2S), \tag{8}$$

where $A^{ij} = K^{ij} = \psi^{-4}(\partial^i\beta^j + \partial^j\beta^i - \frac{2}{3}\delta^{ij}\partial_k\beta^k)/2\alpha$, and the source terms of matter are defined by $\rho_{\rm H} \coloneqq T_{\alpha\beta}n^\alpha n^\beta$, $j^i \coloneqq -T_{\alpha\beta}\gamma^{i\alpha}n^\beta$, and $S \coloneqq T_{\alpha\beta}\gamma^{\alpha\beta}$.

The above set of equations must be supplied with boundary conditions at infinity. Since we are working in the inertial frame and we impose asymptotic flatness, we must have

$$\lim_{r\to\infty}\psi = 1, \qquad \lim_{r\to\infty}\alpha = 1, \qquad \lim_{r\to\infty}\beta^i = 0. \tag{9}$$

B. Hydrostatic equilibrium

The hydrostatic equation for a perfect fluid in quasiequilibrium can be derived from the relativistic Euler equation [62]

$$u^\beta\nabla_\beta(hu_\alpha) + \nabla_\alpha h = 0, \tag{10}$$

where $u^\alpha = u^t(1, v^i) = u^t(1, \Omega\phi^i)$ is the four-velocity of the fluid, with $\phi^i = (-y, x, 0)$, and h is the specific enthalpy defined by $h \coloneqq (\epsilon + p)/\rho$ (ρ is the rest-mass density and ϵ the total energy density).

When the symmetry along a helical Killing vector $k^\alpha = t^\alpha + \Omega\phi^\alpha$ is imposed for the fluid variables, which is approximately true also in the case for a rotating nonaxisymmetric star in quasiequilibrium, the integral of the Euler equation becomes

$$\frac{h}{u^t} = \mathcal{E}, \tag{11}$$

where $\mathcal{E}$ is a constant. From the normalization of the four-velocity $u_\alpha u^\alpha = -1$, one obtains

$$u^t = \frac{1}{\sqrt{\alpha^2 - \omega_a\omega^a}} = \frac{1}{\sqrt{\alpha^2 - \psi^4\delta_{ab}\omega^a\omega^b}}, \tag{12}$$

where $\omega^a = \beta^a + \Omega\phi^a$. The fluid sources of Eqs. (6)–(8), i.e., $\rho_{\rm H}$, j_a, and S, are defined in terms of the energy-momentum tensor in the previous section. In terms of the fluid and field variables, they can be written as [62]

$$\rho_{\rm H} = \rho[h(\alpha u^t)^2 - q], \tag{13}$$

$$j^i = \rho h\alpha(u^t)^2\gamma^{i\alpha}u_\alpha, \tag{14}$$

$$S = \rho h(\alpha u^t)^2 - \rho h + 3\rho q, \tag{15}$$

in which $q \coloneqq p/\rho$ is the relativistic analogue of the Emden function. Here u^t is related to h through Eq. (11). Therefore, in order to close the system, an additional relationship is needed between the specific enthalpy, the pressure, and the rest-mass density of the fluid, i.e., an EOS. Once such a relation is available, to solve the field equations [Eqs. (6)–(8)] and the hydrostatic equation [Eq. (11)] one has to find the two constants $\{\Omega, \mathcal{E}\}$ that appear in all of them. This procedure is described in detail, for example, in Ref. [60].

C. Equation of state

In this work, we have considered two types of EOS for QSs. One of them is the MIT bag-model EOS [66], since it is the most widely used EOS for QSs. In the case when strange quark mass is neglected, the pressure is related to total energy density according to

$$p = \sigma(\epsilon - \epsilon_s), \tag{16}$$

where σ, ϵ_s are two constants, the second being the total energy density at the surface. Related to ϵ_s is the so-called bag constant, $B = \epsilon_s/4$. In this work, and following [67], the simplest MIT bag-model EOS has been employed, where $\sigma = 1/3$ and $B^{1/4} = 138$ MeV.

Besides the MIT bag-model EOS, we have also considered another QS EOS suggested by Lai and Xu [68], which we will refer to as the LX EOS hereafter. Unlike the conventional QS models (e.g., the MIT bag-model EOS) which are composed of deconfined quarks, Lai and Xu [68] suggested that quark clustering is possible at the density of a cold compact star since the coupling of strong interaction is still decent at such an energy scale. Due to the nonperturbative effect of strong interaction at low energy scales and the many-body problem, it is very difficult to derive the EOS of such a quark-cluster star[1] from first principles.

Lai and Xu attempted to approach the EOS of such a quark-cluster star with phenomenological models, i.e., to compare the intercluster potential with the interaction between inert molecules (a similar approach has also been discussed in [70]). They also take the lattice effects into account as the potential could be deep enough to trap the quark clusters. Combining the intercluster potential and the lattice thermodynamics, they have derived an EOS in the following form:

[1]Such a quark-cluster star has also been named a *strangeon* star in Ref. [69].

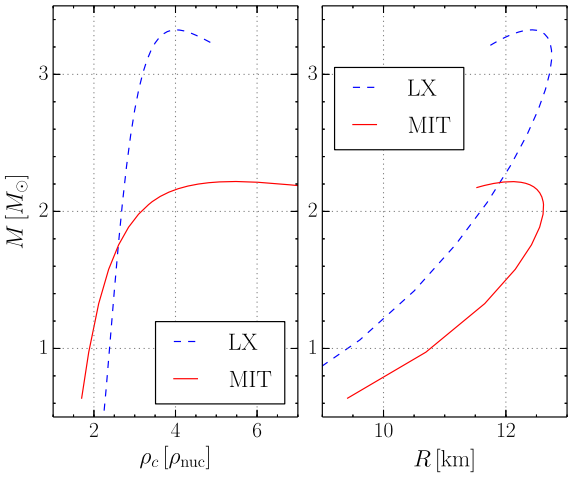

FIG. 1. The Tolman-Oppenheimer-Volkoff (TOV) solution sequences for the MIT bag-model EOS (red solid line) and LX EOS (blue dashed line), respectively. The left panel shows the mass-central density relationship for each model and the right panel is the mass-radius diagram. The bag constant we apply in this work for the MIT bag-model EOS satisfies the two-solar-mass constraint from observations.

$$p = 4U_0(12.4r_0^{12}n^5 - 8.4r_0^6n^3) + \frac{1}{8}(6\pi^2)^{\frac{1}{3}}\hbar c n^{\frac{4}{3}}, \quad (17)$$

where $\hbar$ is the reduced Planck constant. The parameters in this expression, U_0 and r_0, are the depth of the potential and characteristic range of the interaction, respectively. The EOS is also dependent on the number of quarks in each cluster ($N_{\rm q}$) since it relates the energy density (ϵ) and rest-mass density (ρ) to the number density of quark clusters [n in Eq. (17)]. Similarly to the MIT bag-model EOS case, we use the rest-mass density parameter, which is

$$\rho = m_{\rm u}\frac{N_{\rm q}}{3}n, \quad (18)$$

where $m_{\rm u} = 931\ \mathrm{MeV}/c^2$ is the atomic mass unit. While several different choices of parameters are considered in Ref. [68], in our work we restrict our attention to $U_0 = 50$ MeV and for $N_{\rm q} = 18$. We also note that although it is not as obvious as for the MIT bag-model EOS, the LX EOS also has a nonzero surface density since Eq. (17) has a unique zero root when the number density is positive.

Being a stiff EOS, the LX EOS is favored by the discovery of massive pulsars [71–73]. The rest-mass density and mass-radius relationships for spherical models can be seen in Fig. 1, and the characteristics of the maximum mass models are reported in Table I. The LX EOS has also been discussed in relation with the possibility of understanding some puzzling observations related to compact stars, such as the energy release during pulsar glitches [74], the peculiar x-ray flares [75], and the optical/UV excess of X-ray-dim isolated NSs [76]. Particularly, a solid QS model has been suggested in order to understand those observations [77]. However, as pointed out in [74], the critical strain of such a star is very small. A starquake will be induced when the relative difference in ellipticity is 10^{-6}, for most, between the actual configuration of the star and the configuration as if the star were a perfect fluid. This is consistent with the pulsar glitch observations on Vela. Therefore, we find it a good approximation to calculate the quasiequilibrium configuration of such a star with perfect fluid assumption.

TABLE I. Pressure, energy density, rest-mass density, gravitational mass, and compactness at the maximum mass of spherical solutions for the two EOSs in this work. $G = c = M_\odot = 1$ unit is used. To convert to cgs units, use the fact that $1 = 1.477\mathrm{km} = 4.927 \times 10^{-6}\mathrm{s} = 1.989 \times 10^{33}\mathrm{g}$

EOS	$(p/\rho)_c$	ϵ_c	ρ_c	M	$\mathcal{C}$
MIT	0.2940	2.609×10^{-3}	2.342×10^{-3}	2.217	0.2706
LX	2.326	2.451×10^{-3}	1.744×10^{-3}	3.325	0.3956

Understanding the models and properties of the QS EOSs that we want to consider, we can modify the EOS part of the simulation code, which was originally designed for NS models, accordingly.

As mentioned above, in the case of NSs, a piecewise-polytropic EOS is usually assumed to describe the EOS [62,78]. In each piece, the pressure and rest-mass density are related as

$$p_i = \kappa_i\rho^{\Gamma_i} = \kappa_i\rho^{1+1/n_i}, \qquad i = 1, 2, \ldots, N. \quad (19)$$

For QSs, due to the nonzero surface density and nonzero energy density integration constant, we will assume that the EOS is generally a polynomial,

$$p = \sum_{i=1}^{N}\kappa_i\rho^{\Gamma_i}. \quad (20)$$

Given the relationship between p and ρ, one can apply the first law of thermodynamics to obtain other quantities such as the energy density and the specific enthalpy. In the zero-temperature case, the first law of thermodynamics can be expressed as [62]

$$d\epsilon = \frac{\epsilon + p}{\rho}d\rho \quad \text{or} \quad d\left(\frac{\epsilon}{\rho}\right) = \frac{p}{\rho^2}d\rho, \quad (21)$$

which can be integrated to obtain the total energy density. The integral constant is usually chosen to be 1, since when there is no internal energy, the energy density and the rest-mass density coincide (apart from the square of the speed of light). However, for QS EOSs (like in [70] and the MIT bag-model EOS), the integral constant is different from unity and needs to be properly taken into account.

In this case, the energy density and specific enthalpy are related to the rest-mass density by

$$\epsilon = \sum_{i=1}^{N} \frac{\kappa_i}{\Gamma_i - 1} \rho^{\Gamma_i} + \rho(1 + C), \tag{22}$$

$$h = \frac{\epsilon + p}{\rho} = \sum_{i=1}^{N} \frac{\Gamma_i \kappa_i}{\Gamma_i - 1} \rho^{\Gamma_i - 1} + 1 + C. \tag{23}$$

Here C is the integral constant we mentioned above. It is usually taken to be zero for NS models. Here it is introduced again in order to accommodate stars that have different surface limits for the thermodynamic variables.

The nonzero surface density of QSs requires a different boundary condition in our simulation. For typical NSs when we adjust the position of the surface, we are actually locating the points where the specific enthalpy is 1. For QSs, the surface identification will be at values of the specific enthalpy different from unity and consistent with Eq. (23). What we typically use as the input parameter is the surface rest-mass density ρ_s, from which we then calculate h_s using Eq. (23).

As an example, for the MIT bag-model EOS the first law at zero temperature implies

$$\epsilon = \frac{1}{1 + \sigma} (\bar{C} \rho^{1+\sigma} + \sigma \epsilon_s), \tag{24}$$

$$p = \frac{\sigma}{1 + \sigma} (\bar{C} \rho^{1+\sigma} - \epsilon_s), \tag{25}$$

$$h = \bar{C} \rho^{\sigma}, \tag{26}$$

where $\bar{C}$ is a constant of integration. The above EOS is of the form (20) with

$$\kappa_1 = \frac{\sigma \bar{C}}{1 + \sigma}, \qquad \Gamma_1 = 1 + \sigma,$$
$$\kappa_2 = -\frac{\sigma \epsilon_s}{1 + \sigma}, \qquad \Gamma_2 = 0, \tag{27}$$

and $C = -1$. Having all thermodynamical variables in terms of the rest-mass density is convenient from the computational point of view since this is one of the fundamental variables used in the COCAL code; therefore, the modifications with respect to the EOS will be minimal.

Given a fixed choice of σ and B for the MIT bag-model EOS, one can obtain a unique solution of the field equations under hydrostatic equilibrium (see Secs. II A and II B). In other words, the relationship between the gravitational mass versus the central energy density, the mass-radius relationship, and the spacetime metric will not depend on the coefficient $\bar{C}$, as it is eliminated from Eq. (16) (a similar argument can be found in [79,80]). At the same time, it will indeed affect the rest mass and, hence, the binding energy of the QS, since it relates the rest-mass density and the number density of the components. Hence, a reasonable choice for $\bar{C}$ will still be helpful, although it will not affect anything that we are interested in for this work. Here we choose $\bar{C}$ such that the EOS corresponds to the $a_4 = 0.8$ model as in [81] and we assume a rest mass of 931 MeV$/c^2$ for each baryon number ($n_b = n_q/3$, where n_q is the number density of quarks). Any other choices for $\bar{C}$ are in principle possible and they will not affect our solution except for the rest mass of the star. Actual values of these constants can be found in Table II in cgs units.

In Eqs. (24) and (25) we have employed a relationship which is quite similar to the explicit form of the MIT bag model. By factoring out the rest mass, those two equations can be rewritten as a function of number density instead of rest-mass density. However, one clarification we want to discuss at this point is that the choice of using Eqs. (24) and (25) is not essential. Moreover, Eqs. (24) and (25) are related by the first law of thermodynamics [see Eq. (21)], which is not essential either. We can describe the MIT EOS Eq. (16), in a parametric form $(p(\rho), \epsilon(\rho))$ with an arbitrary parameter ρ, as long as the functions $p(\rho)$ and $\epsilon(\rho)$ satisfy Eq. (16). In doing so we choose to satisfy Eq. (21) and therefore arrive at Eqs. (24) and (25). As one can see from Eqs. (13)–(15), the fluid terms that appear are $q\rho = p$ and $h\rho = \epsilon + p$. Thus, for the MIT bag-model EOS, the only thermodynamic variable that appears in the field equations is ϵ. Every model thus calculated will be uniquely defined by a deformation parameter and the central total energy density. The scaling constant, which is analogous to scaling as $\kappa^{n/2}$ for NSs [62], is here $\epsilon_s^{-1/2}$.

TABLE II. Quark EOS parameters in cgs units for the MIT and LX EOSs, respectively. $\rho_{\rm nuc}$ is the nuclear saturation density which is chosen to be 2.67×10^{14} g cm^{-3}. Unlike NSs which have a surface enthalpy $h_s = 1$, for QSs this value is an input parameter for a specific model. In practice one inputs the rest-mass density at the surface ρ_s and then h_s is computed from the EOS. The constant C is the integration constant of the first law and determines the limit of the thermodynamic variables at the surface of the star.

MIT bag-model EOS		
$C = -c^2$	$\rho_s = 1.4\rho_{\rm nuc}$	$h_s = 0.896\,974\,78c^2$
$N = 2$	κ_i	Γ_i
$i = 1$	$2.797\,790\,7 \times 10^{15}$	$\frac{4}{3}$
$i = 2$	$-7.527\,976\,8 \times 10^{34}$	0
LX EOS		
$C = 0$	$\rho_s = 2.0\rho_{\rm nuc}$	$h_s = 0.968\,286\,75c^2$
$N = 3$	κ_i	Γ_i
$i = 1$	$2.082\,470\,6 \times 10^{-39}$	5
$i = 2$	$-6.155\,937\,5 \times 10^{-10}$	3
$i = 3$	$7.130\,722\,6 \times 10^{13}$	$\frac{4}{3}$

Before concluding this discussion on the EOSs, we should mention that although a polynomial-type EOS is implemented for the calculation of QSs with a finite surface density, the developments in the new version of COCAL allow us to calculate any compact star with an EOS that can be described by a polynomial function, including NSs and hybrid stars. For instance, some phenomenological approaches suggested recently in Ref. [82] also result in a polynomial-type EOS, which can be computed straightforwardly with the new code.

III. CODE TESTS

The working properties of the COCAL code for single rotating stars is presented in detail in previous works, e.g., [37,38],[2] so that here we will only mention the most important quantities that are used in our simulations. The method has its origins in the works of Ostriker and Mark [83], who used it to compute Newtonian stars, and the works of Komatsu *et al.* [84], who devised a stable numerical algorithm and obtained first axisymmetric general-relativistic rotating stars. From this latest work, the method is commonly referred to as the KEH method and consists of an integral representation of the Poisson equation commonly referred to as the representation formula. Since we have only one computational domain with trivial boundary conditions at infinity, the Green's function is $G(x,x') = 1/|x-x'|$ and is expanded as a series of the associated Legendre polynomials and trigonometric functions. The maximum number of terms included in this expansion is given as L in Table III.

This approach is used to compute the gravitational fields $\{\alpha, \psi, \beta^i\}$ while hydrostatic equilibrium is achieved through Eq. (11). At every step in the iteration to reach the solution at the desired accuracy, three constants need to be computed. The first one is the angular velocity of the star, Ω; the second one is the constant from the Euler integral, $\mathcal{E}$, in Eq. (11); and, finally, the third constant is R_0, a normalization factor for the whole domain where the equations are solved.[3] At every step during the iteration, the nonlinear equation with respect to these three constants is solved typically by evaluating Eq. (11) at three points in the star. For axisymmetric configurations, we use the center of the star and two points on the surface, one on the positive x-axis and one at the North pole of the stellar model. An axisymmetric equilibrium is achieved by setting the ratio between the polar axis over the equatorial radius along the x-axis. For triaxial configurations, on the other hand, the three points are the center of the star together with two points again on the surface, one at the positive x-axis, and one on the positive y-axis. Each triaxial solution has a fixed ratio of the radius on the y-axis over the radius of the x-axis.

From a numerical point of view, COCAL is a finite-difference code that uses spherical coordinates $(r,\theta,\phi) \in [0,r_b]\times[0,\pi]\times[0,2\pi]$[4] and the basic parameters are summarized in Table III. In the angular directions θ,ϕ, the discretization is uniform, i.e., $\Delta\theta = \pi/N_\theta$ and $\Delta_\phi = 2\pi/N_\phi$. In the radial direction, the grid is uniform until point r_c with $\Delta r_i = r_c/N_r^{\rm m}$, and in the interval $[r_c, r_b]$ the radial grid is nonuniform and follows a geometric series law [37]. While field variables are evaluated at the gridpoints, source terms under the integrals are evaluated at midpoints between two successive gridpoints since the corresponding integrals use the midpoint rule. For integrations in r and ϕ, we use a second-order midpoint rule. For integrations in θ we use a fourth-order midpoint rule. This was proven necessary to keep second-order convergence at the region of maximum field strength [58]. Derivatives at midpoints are calculated using a second-order rule for the angular variables θ,ϕ, and a third-order rule for the radial variable r (again for keeping second-order convergence in the same regions [57]). Derivatives evaluated at gridpoints always use a fourth-order formula in all variables.

It is worth noting that, since for QSs the relationship between the specific enthalpy and the rest-mass density follows a general polynomial function [cf., Eq. (23)], a root-finding method needs to be employed when calculating the thermodynamical quantities from the enthalpy. The regular polynomial expression of the specific enthalpy with respect to rest-mass density allows us to use a Newton-Raphson method as the derivative can also be expressed easily. In view of this, the computational costs with a QS EOS are not significantly larger than those with a NS EOS. However, in order to guarantee a solution of rest-mass density when the specific enthalpy is given, a bisection root-finding method needs to be employed if the Newton-Raphson method does not converge sufficiently rapidly. In this case, the initial range of the bisection method is set to be the specific enthalpy corresponding to the rest-mass densities at the stellar center and at the surface, respectively.

In previous works [37,38,58,85], the COCAL code has been extensively tested, both with respect to its convergence properties and with respect to actual evolutions with other well-established codes [85].

In what follows we report the convergence tests we have performed in order to investigate the properties of the code under these new conditions. Before doing that, we note that special care is needed when using a root-finding method to calculate thermodynamical quantities for a given specific enthalpy in the case of rotating QSs. In particular, it is crucial to consider what the accuracy set is during the root-finding step. Of course, it is possible to require that the

[2]See [57–60] for the general binary case.

[3]We recall that COCAL uses normalized variables $\hat{x}^i := x^i/R_0$. The quantities listed in Table IV refer to those and should be denoted by a hat. For simplicity, however, we have omitted these hats in the table.

[4]Note that the field equations for the shift vector Eq. (7) are expressed in Cartesian coordinates.

TABLE III. Summary of parameters used for rotating star configurations.

r_a: Radial coordinate where the grid r_i starts.
r_b: Radial coordinate where the grid r_i ends.
r_c: Radial coordinate between r_a and r_b where the grid changes from equidistant to nonequidistant.
N_r: Total number of intervals Δr_i between r_a and r_b.
$N_r^{\rm m}$:Number of intervals Δr_i in $[0, r_c]$.
$N_r^{\rm f}$: Number of intervals Δr_i in $[0, R(\theta,\phi)]$.
N_θ: Total number of intervals $\Delta\theta_i$ for $\theta \in [0,\pi]$.
N_ϕ:Total number of intervals $\Delta\phi_i$ for $\phi \in [0, 2\pi]$.
L: Number of multipoles in the Legendre expansion.

accuracy in the root-finding step be much higher than the other convergence criteria in the code to guarantee an accurate result. In this way, however, the computational costs will increase considerably, since the thermodynamical quantities need to be calculated at every gridpoint and at every iteration. We found that an accuracy of 10^{-10} for the thermodynamic variables solutions neither compromises the accuracy of the solutions nor slows down the code significantly.

A. Comparison with rotating NSs

Although the newly developed code presented here is intended for QS EOSs, it can also be used to produce rotating NSs if one restricts the EOS to a single polytrope. This can be accomplished by setting the polynomial terms to be only 1, the surface rest-mass density $\rho_s = 0$ and the energy integral constant $C = 0$. In this case, Eq. (20) becomes

$$p = \kappa\rho^{\Gamma} = \kappa\rho^{1+1/n}, \tag{28}$$

and the relationship between the energy density, the specific enthalpy, and the rest-mass density [Eqs. (22) and (23)] will be exactly the same as that for a polytropic NS.

We choose a stiff EOS with $n = 0.3$ and produce axisymmetric solution sequences for small and high compactness $\mathcal{C} \coloneqq M_{\rm ADM}/R = 0.1$, 0.2, and $M_{\rm ADM}$ is the corresponding Arnowitt-Deser-Misner (ADM) mass for a nonrotating model, both with the original rotating-NS and the modified rotating-QS solver. The grid-structure parameters used are $N_r = 240$, $N_r^{\rm m} = 80$, $N_r^{\rm f} = 64$, $N_\theta = 96$, $N_\phi = 192$, $L = 12$, $r_b = 10^4$, and $r_c = 1.25$ (see Table III). Overall, we have found that the relative difference in all physical quantities is of the order of 10^{-6}, which is what is expected since the criteria for convergence in COCAL are that the relative difference in metric and fluid variables between two successive iterations is less than 10^{-6}.

B. Convergence test for rotating QSs

For the convergence analysis in this work we use the five resolutions shown in Table IV. The outer boundary of the domain is placed at $r_b = 10^6$, while the surface of the star is always inside the sphere $r = 1$. The radius along the x-axis is exactly $r = 1$ in the normalized variables. There are exactly $N_r^{\rm f}$ intervals along the radii in the x, y, and z directions. The number of Legendre terms used in the expansions is kept constant ($L = 12$) in all resolutions since convergence with respect to those has already been investigated in [86]. When going from the low-resolution setup H2.0 to the high-resolution one H4.0, the spacings $\Delta r, \Delta\theta, \Delta\phi$ decrease as $2/3, 3/4, 2/3, 3/4$.

TABLE IV. Five different resolutions used for convergence tests. Parameters are shown in Table III. The number of points that covers the largest star radius is $N_r^{\rm f}$.

Type	r_a	r_b	r_c	N_r	$N_r^{\rm m}$	$N_r^{\rm f}$	N_θ	N_ϕ	L
H2.0	0	10^6	1.25	192	80	64	48	48	12
H2.5	0	10^6	1.25	288	120	96	72	72	12
H3.0	0	10^6	1.25	384	160	128	96	96	12
H3.5	0	10^6	1.25	576	240	192	144	144	12
H4.0	0	10^6	1.25	768	320	256	192	192	12

As a result, if we denote as f_μ, f_ν a quantity evaluated at two different resolutions, then

$$f_\mu - f_\nu \approx A\left[\left(\frac{\Delta_\mu}{\Delta_\nu}\right)^n - 1\right]\Delta_\nu^n, \tag{29}$$

where A is a constant and Δ_μ is the grid separation at resolution Hμ. Choosing the combinations $f_{\rm H3.0} - f_{\rm H2.0}$, $f_{\rm H3.5} - f_{\rm H2.5}$, and $f_{\rm H4.0} - f_{\rm H3.0}$ so that we have $\Delta_\mu/\Delta_\nu = 1/2$ and normalizing by $f_{\rm H4.0}$, we plot in Fig. 2 the relative error with respect to the grid spacing for Ω, $M_{\rm ADM}$, J, $T/|W|$, M_0, and the eccentricity $e \coloneqq \sqrt{1-(\bar{R}_z/\bar{R}_x)^2}$, both for the LX EOS (left panel) and for the MIT bag-model EOS (right plot). The deformation is kept at $R_z/R_x = 0.75$ for both EOSs, while the central densities are $\epsilon_c = 1.301 \times 10^{-3}$ and $\epsilon_c = 7.361 \times 10^{-4}$ for the LX and MIT bag-model EOS, respectively. The dashed black line reports a reference first-order convergence, while the solid black line refers to a second-order convergence.

Note that quantities like the ADM mass, the angular velocity and the eccentricity converge to second order, while quantities like the angular momentum, the ratio $T/|W|$, and the rest mass converge to an order that is closer to first. Furthermore, Fig. 2 shows that some quantities (e.g., the ADM mass of the LX EOS) show a convergence order that is larger than second, but this is an artifact of the specific deformation. In general, we found second-order convergence in $M_{\rm ADM}, \Omega$, and e, and at least first order for $J, T/|W|$, and M_0.

Note also that the two panels in Fig. 2 are very similar, even though the EOSs are quite different, with the MIT bag-model EOS being relatively soft (i.e., $p \propto \rho^{4/3}$), while the LX EOS is comparatively stiff (i.e., $p \propto \rho^5$). Hence, the

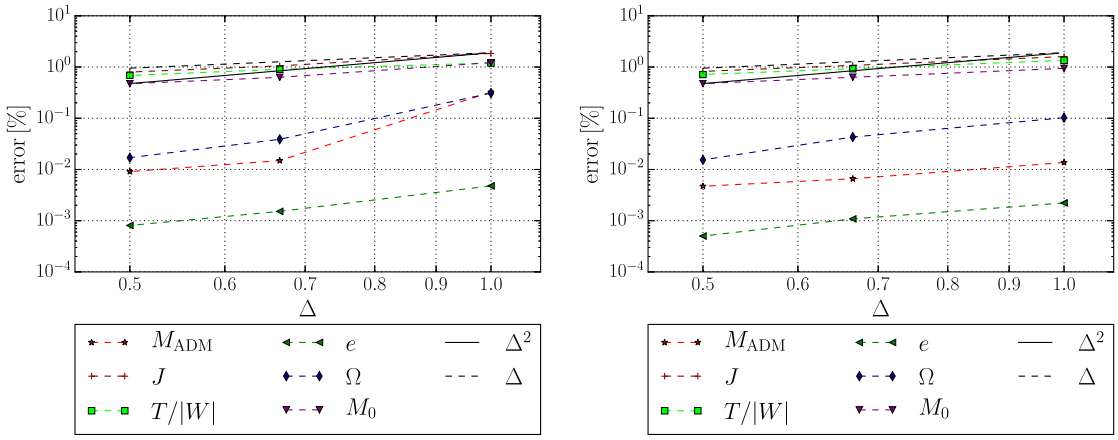

FIG. 2. Normalized differences $|(f_{\rm H3.0}-f_{\rm H2.0})/f_{\rm H4.0}|$, $|(f_{\rm H3.5}-f_{\rm H2.5})/f_{\rm H4.0}|$, and $|(f_{\rm H4.0}-f_{\rm H3.0})/f_{\rm H4.0}|$ are plotted for Ω, $M_{\rm ADM}$, J, $T/|W|$, M_0, and $e \coloneqq \sqrt{1-(\bar{R}_z/\bar{R}_x)^2}$ against the resolutions $\Delta_{\rm H3.0}$, $\Delta_{\rm H2.5}$, and $\Delta_{\rm H2.0}$. The black solid line is proportional to Δ^2, while the black dashed line is proportional to Δ. The left panel refers to the LX EOS (Table II) with central rest-mass density $\epsilon_c = 1.301 \times 10^{-3}$ and axis ratio in the coordinate length $R_z/R_x = 0.75$. The right panel is the same but for the MIT bag-model EOS with $\epsilon_c = 7.361 \times 10^{-4}$ and the same deformation as the LX plot.

overall larger error that is reported in Fig. 2 when compared to the corresponding Fig. 1 in Ref. [37] is mostly due to the finite rest-mass density at the stellar surface. In the original rotating-NS code, in fact, the surface was determined through a first-order interpolation scheme. This approach, however, is not sufficiently accurate for rotating QSs and would not lead to the desired convergence order unless the surface finder scheme was upgraded to second order.

IV. TRIAXIAL SOLUTIONS

The onset of a secular instability to triaxial solutions for the MIT bag-model EOS stars has been studied previously via a similar method in Ref. [56]. Surface-fitted coordinates have been used to accurately describe the discontinuous density at the surface of the star, and a set of equations similar to the one of the conformal flat approximation used here was solved. In order to find the secular bar-mode instability point, the authors of Ref. [56] performed a perturbation on the lapse function of an axisymmetric solution and built a series of triaxial quasiequilibrium configurations to see whether this perturbation is damped or grows.

Here, we build quasiequilibrium sequences with constant rest mass (axisymmetric and triaxial) for both the MIT bag-model EOS and the LX EOS. We begin with the axisymmetric sequence in which we calculate a series of solutions with varying parameters, i.e., the parameters that determine the compactness (e.g., the central rest-mass density ρ_c) and the rotation (R_z/R_x). In doing so, we impose axisymmetry as a separate condition and manage to reach eccentricities as high as $e \simeq 0.96$ for $R_z/R_x = 0.2656$ and compactness $\mathcal{C} = 0.1$. In order to access the triaxial branch of solutions, we recompute the above sequence of solutions but this time *without* imposing axisymmetry. As the rotation rate increases (R_z/R_x decreases), the triaxial deformation ($R_y/R_x < 1$) is *spontaneously* triggered, since at a large rotation rate the triaxial configuration possesses lower total energy and is therefore favored over the axisymmetric solution. This approach is different from the approach followed in Ref. [17], where the triaxial $m = 2$ perturbation was triggered after a suitable modification of a metric potential.

We keep decreasing R_z/R_x to reach the mass-shedding limit with the triaxial configuration. We can then move along the triaxial solution sequence by increasing R_y/R_x, which now acts as the new rotating parameter. The sequence is then terminated close to the axisymmetric sequence. The bifurcation point can be found by extrapolating this triaxial sequence towards the axisymmetric solutions. The largest triaxial deformation calculated in this work, for both the MIT bag-model EOS and the LX EOS, is $R_y/R_x = 0.5078$ for the $\mathcal{C} = 0.1$ case (a three-dimensional image of the surface for this solution is shown in Fig. 3), $R_y/R_x = 0.5234$ for $\mathcal{C} = 0.15$, and $R_y/R_x = 0.6757$ for $\mathcal{C} = 0.2$. Similar to NSs [37], the end point of the triaxial sequence happens in lower eccentricities as the compactness increases.

In Figs. 4 and 5, the relation between the $T/|W|$ ratio versus the eccentricity of the star has been plotted for three different compactnesses ($\mathcal{C} = 0.1, 0.15$, and 0.2) for both the MIT bag-model EOS and the LX EOS. Unlike in a Newtonian incompressible star, for which the bifurcation to triaxial deformation happens at $(T/|W|)_{\rm crit,Newt} \simeq 0.1375$ for any compactness, in general relativity the bifurcation point depends on the compactness. According to [17],

$$\left(\frac{T}{|W|}\right)_{\rm crit} = \left(\frac{T}{|W|}\right)_{\rm crit,Newt} + 0.126\mathcal{C}(1+\mathcal{C}). \quad (30)$$

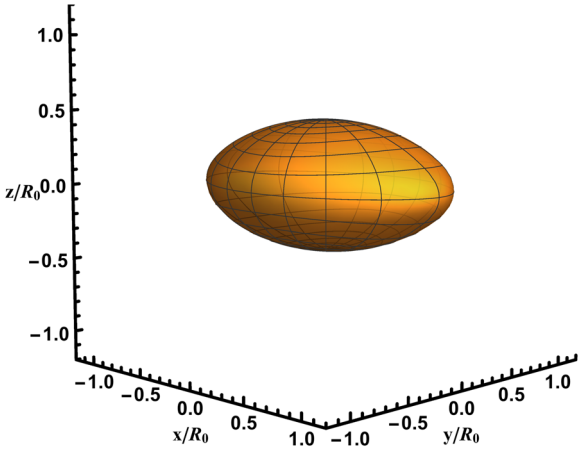

FIG. 3. Illustration of the three-dimensional surface of a QS solution with the largest triaxial deformation for the MIT bag model with corresponding spherical compactness $\mathcal{C} = 0.2$. The axis ratio R_y/R_x is 0.6757 and $R_z/R_x = 0.4375$. The solid black lines on the surface correspond to fixed values of the latitude angle and the fact that they are not parallel is a result of the triaxial deformation.

This relation holds true not only for NSs but also for QSs with the MIT bag-model EOS (see Fig. 1 of [56]). The largest $T/|W|$ for the onset of secular instability is found to be $\simeq$0.17 for rotating QSs in the configurations that we considered for both the MIT bag-model EOS and the LX EOS, and it will be even larger for higher compactnesses. Both the LX EOS and the MIT bag-model EOS in our calculations follow this relationship within a maximum error of 3%. This implies that the secular instability to a "Jacobi-type" ellipsoidal figure in general relativity is not particularly affected by the stiffness of the EOS for quark matter.

It is worth noting that when compared with the rotating NSs calculated in Ref. [38], rotating QSs have longer triaxial sequences. In other words, the triaxial sequence of rotating QSs terminates at larger eccentricity as well as larger triaxial deformation (in other words, smaller R_y/R_x ratio). A rotating NS with $\Gamma = 4$ and compactness $\mathcal{C} = 0.1$ bifurcates from axisymmetry at $e \simeq 0.825$ and can rotate fast enough to reach eccentricities $e < 0.9$ (see Fig. 6 in [38]). For the QS models considered here and both EOSs, we have a bifurcation point at $e \simeq 0.825$ and the mass-shedding limit at $e \simeq 0.93$. For more compact NSs with $\mathcal{C} = 0.2$, the bifurcation point happens at $e \simeq 0.835$ and the mass shedding limit at $e \simeq 0.88$. The corresponding compactness QS models bifurcate at $e \simeq 0.83$ and rotate as fast as $e \simeq 0.89$.

A few remarks are useful to make at this point. First, we note that these values of eccentricity are strictly valid under the assumption of the conformal flatness approximation, which is however accurate for smaller compactnesses. These estimates are less accurate when the compactness increases and are slightly different when adopting more accurate formulations, such as the waveless approximation (see Fig. 6 in [38]). Second, another difference between triaxial NSs and QSs is that for triaxial NSs, the ratio $T/|W|$ is essentially constant along the triaxial sequence, especially for higher compactnesses (for lower compactnesses there is an increase towards the mass-shedding limit, but this is very slight). For rotating triaxial QSs, on the other hand, although this qualitative behavior is still true, a greater curvature towards higher $T/|W|$ ratios can be seen. For example, for the $\mathcal{C} = 0.1$ models mentioned above, the difference between the critical value of $T/|W|$ and the one at the mass-shedding limit is $(T/|W|)_{\rm ms} - (T/|W|)_{\rm crit} \simeq 0.0015$ for NSs while it is

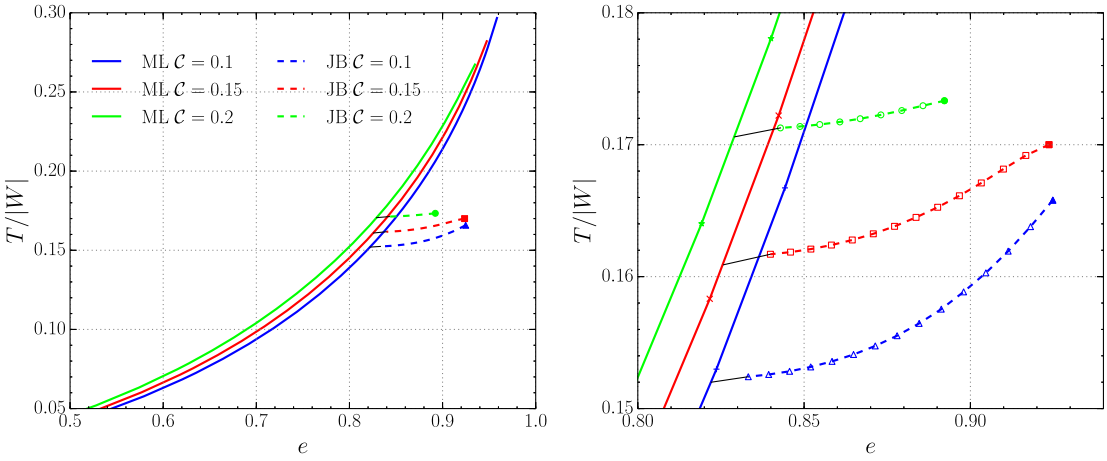

FIG. 4. Left: $T/|W|$ versus eccentricity $e := \sqrt{1-(\bar{R}_z/\bar{R}_x)^2}$ (in proper length) for MIT bag-model EOS sequences. Solid curves are axisymmetric solution sequences and dashed curves are triaxial solution sequences that correspond to $\mathcal{C} = M/R = 0.2$ (green curves), 0.15 (red curves), and 0.1 (blue curves), respectively. Note that M is the spherical ADM mass. Right: Magnification of the region near the onset of the triaxial solutions marked with empty symbols, while filled symbols mark the models at the mass-shedding limit. Solutions labeled with ML are axisymmetric solutions (Maclaurin spheroids), while those labeled JB are triaxial solutions (Jacobi ellipsoids).

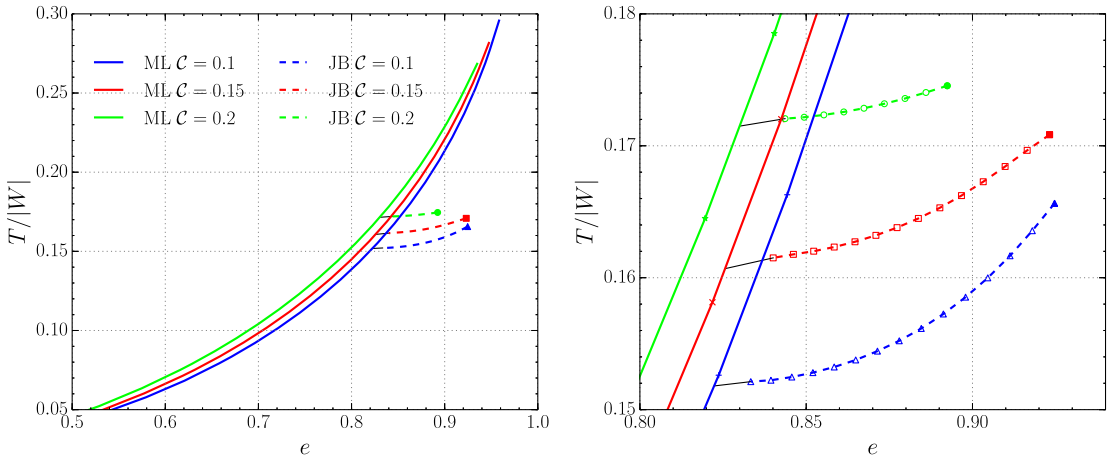

FIG. 5. The same as Fig. 4 but for the LX EOS sequences.

0.0137 for QSs. Third, in Ref. [56] it has been shown that at the bifurcation point the relation between the scaled angular frequency, $f/\bar{\epsilon}_s^{1/2}$, where $\bar{\epsilon}_s = \epsilon_s/(c^2 10^{14}\ \mathrm{g\,cm^{-3}})$, and the scaled gravitational mass $M_{\mathrm{ADM}}\bar{\epsilon}_s^{1/2}$ depends only very weakly on the bag constant. If we consider models with the compactness $\mathcal{C} = 0.1$ model (see top line in Table V), $M_{\mathrm{ADM}}\bar{\epsilon}_s^{1/2} = 1.193\ M_\odot$ and $f/\bar{\epsilon}_s^{1/2} = 495.9$ Hz, while the scaled bifurcation frequency for such a scaled mass model is roughly 492–494 Hz as deduced from Fig. 7 in [56]. Similarly, for the $\mathcal{C} = 0.15$ models, the renormalized ADM mass and frequency are $2.140\ M_\odot$ and 527.2 Hz, while the corresponding range is 523–527 Hz in Ref. [56]; finally, for the $\mathcal{C} = 0.2$ case, the values are $3.168\ M_\odot$ and 565.0 Hz, respectively, while the range 558–566 Hz is found in [56]. Overall, the comparison of these three values shows a very good agreement with the results presented in Fig. 7 of Ref. [56].

In order to understand the rotation properties of the triaxial solutions, we also report quantities such as dimensionless spin and dimensionless angular momentum in Figs. 6–8. The dimensionless spin as a function of the eccentricity for the MIT bag model and LX model are shown in Figs. 6 and 7, respectively. The left panel of Fig. 8 reports the spin angular momentum as a function of the eccentricity for the LX EOS. Similar to $T/|W|$, the angular momentum increases with the eccentricity. The main difference is that the relative positioning of the curves as a function of compactness is reversed when compared with the $T/|W|$ plots. In other words, for a given eccentricity the greatest angular momentum is achieved for the smallest compactness, while the greatest $T/|W|$ for the largest one. This is true both for axisymmetric and triaxial solutions. Also as we can see from the right panel of Fig. 8, more compact objects can reach greater rotational frequencies, while less compact objects can reach larger angular

TABLE V. Quantities at the point of bifurcation of triaxial sequences from axisymmetric ones for the two EOSs considered. The compactness of the spherical star with the same rest mass, i.e. $\mathcal{C}$, is the model parameter. R_x is the equatorial radius, and R_z/R_x is the ratio of the polar to the equatorial radius. Each has two values; one is measured in the coordinate length, and the other in parentheses is measured in proper length. ϵ_c is the energy density at the center of the compact star, Ω is the angular velocity. In the last three rows, we report the bifurcation point of simple polytropes with polytropic index n as computed in [37] for comparison. Note that we have chosen appropriate values for κ such that the TOV maximum mass for those polytropic EOSs reaches $2.5\ M_\odot$. The definitions of M_{ADM}, J, $T/|W|$, and I can be found in Appendix A of [60]. Z_{p} is the polar redshift.

EOS	$\mathcal{C}$	R_x	R_z/R_x	ϵ_c	Ω	M_{ADM}	J	$T/\lvert W\rvert$	I	Z_{p}
MIT	0.1	7.021 (8.077)	0.5647 (0.5693)	6.200×10^{-4}	0.028 08	0.6515	0.4580	0.1520	16.31	0.1343
MIT	0.15	7.962 (9.922)	0.5565 (0.5640)	6.811×10^{-4}	0.029 85	1.169	1.293	0.1609	43.30	0.2231
MIT	0.2	8.415 (11.43)	0.5478 (0.5590)	7.696×10^{-4}	0.031 99	1.731	2.649	0.1706	82.83	0.3308
LX	0.1	5.698 (6.557)	0.5644 (0.5689)	9.144×10^{-4}	0.034 51	0.5312	0.3039	0.1518	8.805	0.1343
LX	0.15	6.515 (8.130)	0.5566 (0.5639)	9.542×10^{-4}	0.036 30	0.9686	0.8850	0.1607	24.38	0.2251
LX	0.2	6.972 (9.528)	0.5469 (0.5574)	9.977×10^{-4}	0.038 38	1.481	1.932	0.1715	50.34	0.3401
$n = 0.3$	0.1	6.624 (7.634)	0.5634(0.5693)	9.221×10^{-4}	0.031 80	0.5841	0.3708	0.1507	11.66	0.1328
$n = 0.3$	0.2	7.312 (9.979)	0.5394(0.5535)	1.243×10^{-3}	0.039 26	1.435	1.835	0.1688	46.72	0.3311
$n = 0.5$	0.1	10.30 (11.83)	0.5461(0.5536)	5.153×10^{-4}	0.021 97	0.8416	0.7644	0.1493	34.80	0.1281

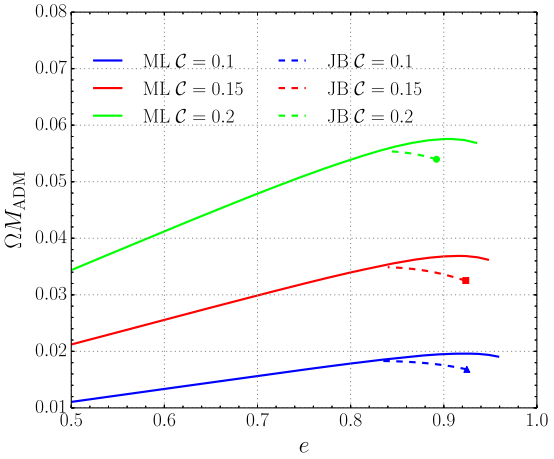

FIG. 6. Plots of $\Omega M_{\rm ADM}$ versus eccentricity for MIT bag-model sequences. Solid curves are axisymmetric solution sequences and dashed curves are triaxial solution sequences that correspond to $\mathcal{C} = M/R = 0.2$ (top green curve), 0.15 (middle red curve), and 0.1 (bottom blue curve), respectively. Note that M is the spherical ADM mass.

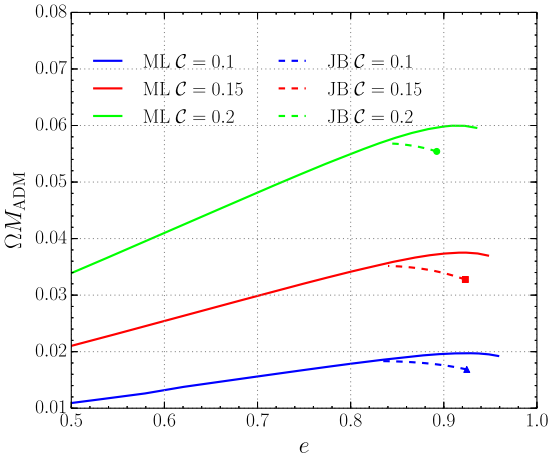

FIG. 7. The same as Fig. 6 but for the LX EOS sequences.

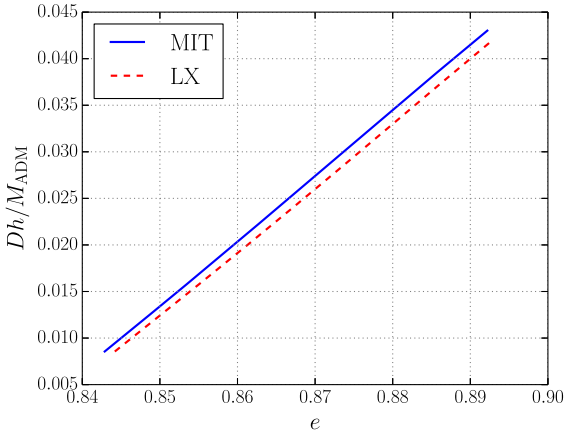

FIG. 9. Estimate of the GW strain amplitude for the $\mathcal{C} = 0.2$ triaxial sequence for both the MIT bag-model EOS (blue solid curve) and the LX EOS (red dashed curve). The quantities are estimated according to the quadrupole formula. Shown is the GW strain for the $\ell = m = 2$ mode normalized by the distance D and the ADM mass $M_{\rm ADM}$ of the source.

momenta, which can exceed unity. According to Figs. 6 and 7, as well as the right panel of Fig. 8, triaxial sequences lose angular velocity and gain spin angular momentum as one moves towards the mass-shedding limit.

An obviously interesting property of triaxially rotating compact stars is that they can act as strong sources of GWs. A full general-relativistic evolution needs to be employed in order to determine accurately the details of the GW emission from such triaxially rotating stars and this is beyond the scope of this paper (see however Ref. [61] for the case of NSs). At the same time, we can apply the quadrupole formula to make reasonable estimates using the quasiequilibrium initial data we have computed. The relationship between the normalized GW strain and the eccentricity of the star is shown in the top panel of Fig. 9. Compared with the results of the triaxially rotating NSs

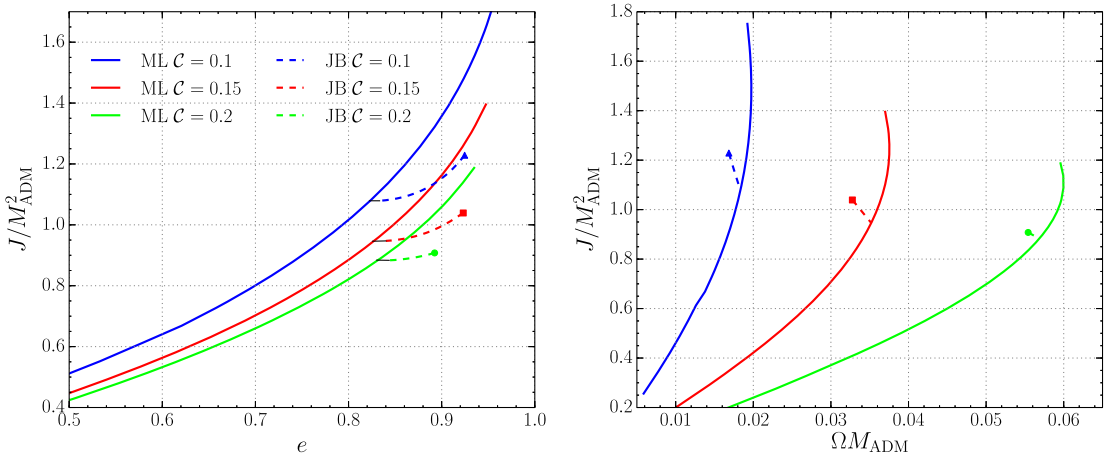

FIG. 8. Spin angular momentum versus the eccentricity and angular velocity for the LX EOS sequences. Dashed curves and solid curves from the top to the bottom in each panel correspond to $\mathcal{C} = 0.2$ (green), 0.15 (red), and 0.1 (blue), respectively.

TABLE VI. Quantities of triaxial supramassive QS solutions with the largest triaxial deformation (smallest R_y/R_x ratio) in our calculations. The above quantities are defined in the same way as in Table V. The TOV maximum mass of each EOS is also shown as a comparison. Because of the limitation of IWM formulation, there might be ∼3% errors on the quantities listed above (see related discussions in Sec. V).

EOS	R_z/R_x	R_y/R_x	R_x	ϵ_c	Ω	$M_{\rm ADM}$	J	$T/\lvert W\rvert$	I	$M_{\rm TOV}$
MIT	0.4375 (0.4713)	0.7657 (0.7938)	9.978 (16.32)	1.259×10^{-3}	0.038 70	2.862	6.847	0.1839	173.1	2.217
LX	0.4375 (0.4912)	0.7586 (0.8104)	7.660 (16.49)	1.348×10^{-3}	0.050 01	3.727	11.30	0.1948	222.1	3.325

calculated in [61], we find that the GW strain for QSs are several times larger for similar values of compactness. For example, model G4C025 in [61] with $e = 0.8685$ radiates GW with normalized strain 0.007 357, while the corresponding amplitude for both the MIT bag-model EOS and the LX EOS is around 0.025 with the same eccentricity (see Fig. 9). Also shown in Fig. 9 for the two EOSs considered are the relations between the strain and the eccentricity, which are very similar and both essentially linear.

V. TRIAXIAL SUPRAMASSIVE SOLUTIONS

Besides the constant rest-mass sequences mentioned above, we have also built sequences with constant central rest-mass density for both the MIT bag-model EOS and the LX EOS. We recall that when fixing the central rest-mass density, the mass of the solutions will increase as the axis ratio R_z/R_x decreases. Furthermore, since we do not impose axisymmetry, the triaxial deformation will be spontaneously triggered when $T/|W|$ is large enough. Therefore, with such calculations we can determine whether triaxial supramassive QSs, i.e., triaxial solutions with ADM mass larger than the TOV maximum mass ($M_{\rm TOV}$) exist and the properties of such solutions.[5] (Note that all models shown in Figs. 4–8 are not supramassive).

According to [89], triaxial supramassive NS does exist for the case with polytropic EOS in the range $\Gamma \gtrsim 4$. Furthermore, for the case with a two-segment piecewise polytropic EOS, sequences of triaxial supramassive NS solutions become longer, and hence the existence of supramassive triaxial NSs becomes evident, when the EOS of the lower density region is stiff ($\Gamma = 4$) and the higher density region is soft ($\Gamma = 2.5$) [89]. Therefore, it is likely that the triaxial supramassive QS also exists because the QS EOS used in this paper has an analogous property; namely, the effective Γ is smaller (softer) in the higher density region and larger (stiffer) in the lower density region (for the MIT model, see [51]). Besides having an interest of its own, determining the existence of such solutions could be relevant to establish whether a BNS merger could lead to the formation of such an object. Based on current mass measurement constraints [72,73] and on known BNS systems, the mass of the postmerger product will very likely be larger than $M_{\rm TOV}$.

In order to study this, we have fixed the central rest-mass density close to the value corresponding to $M_{\rm TOV}$ and built rotating solution sequences for both the MIT bag-model EOS and the LX EOS, respectively. In this way, we were indeed able to find triaxial supramassive solutions for both EOSs, reporting in Table VI the solutions with largest triaxial deformation, i.e., the smallest ratio R_y/R_x.

Finally, we note that although such models have large compactnesses and we are aware that the IWM formalism becomes increasingly inaccurate for large compactnesses (i.e., with $\mathcal{C} \gtrsim 0.3$), we also believe that the associated ∼3% errors will not change the qualitative result, namely, that triaxial supramassive QS models exist for the EOSs considered here. At the same time, we plan to reinvestigate this point in the future, when more accurate methods, such as waveless formulation, will be employed to compute QS solutions.

VI. CONCLUSION

We have presented a new version of the COCAL code to compute axisymmetric and triaxial solutions of uniformly rotating QSs in general relativity with two EOSs, i.e., the MIT bag model and the LX EOS. Comparisons have been made with NSs as well. Overall, three main properties are found when comparing solution sequences of QSs with of NSs. Firstly, QSs generally have a longer triaxial sequences of solutions than NSs. In other words, QSs can reach a larger triaxial deformation (or smaller R_y/R_x ratio) before terminating the sequence at the mass-shedding limit; this is mostly due to the larger $T/|W|$ ratio that can be attained by QSs. Secondly, when considering similar triaxial configurations, QSs are (slightly) more efficient GW sources; this is mostly due to the finite surface rest-mass density and hence larger mass quadrupole for QSs. Thirdly, triaxial supramassive solutions can be found for QSs as well; this is again due to the fact that larger values of the $T/|W|$ ratio can be sustained before reaching the mass-shedding limit.

Besides having an interest of its own within solutions of self-gravitating objects in general relativity, triaxially

[5]We recall that for NSs, a universal relation has been found between $M_{\rm TOV}$ and the maximum mass that can be sustained by axisymmetric solutions in uniform rotation, $M_{\rm max}$ (see also [87] for the case of differentially rotating stars). More specifically, Breu and Rezzolla [88] found that $M_{\rm max} \simeq (1.203 \pm 0.022) M_{\rm TOV}$ for a large class of EOSs; we expect a similar universal behavior to be present also for QSs, although the scaling between $M_{\rm max}$ and $M_{\rm TOV}$ is likely to be different.

rotating compact stars are important sources for ground-based GW observatories. Our calculations have shown that for rotating QSs with different EOSs, the bifurcation point to the triaxial sequence happens at a spin period of ∼1 ms, so that the corresponding GW frequency is ∼2 kHz and hence within the band of GW observatories such as Advanced LIGO or Virgo. Indeed, exploiting the largest triaxial deformation solution obtained in our calculations, the GW strain amplitude can be as large as 10^{-23} at a distance of ∼30 Mpc.

Although this is an interesting prospect, it is still unclear whether such triaxial configurations can be produced in practice, since the radiation-reaction time scales needed for the triggering of the secular triaxial instability are still very uncertain, as are the other mechanisms that could contrast the instability. For example, if the triaxial deformation is induced in an isolated star, e.g., a newly born fast rotating star, GW radiation may take away the excess angular momentum very rapidly so that the star would go back to the axisymmetric sequence again after the $T/|W|$ ratio drops below the critical value. Similarly, when considering stars in binary systems, there is the prospect that an accreting system, such as the one spinning up pulsars, could drive the accreting compact star to exceed the critical $T/|W|$ ratio, hence leading to a break of axisymmetry. In this process, which is also known as forced GW emission, the triaxial deformation can be maintained via the angular momentum supplied by the accreted matter. Notwithstanding the large uncertainties involved with the details of this picture, such as the presence or absence of a bifurcation point or the realistic degree of deformation attained by the unstable stars, the fact that these details depend sensitively on the EOS [89] suggests that a detection of this type of signal could serve as an important probe for distinguishing the EOS of compact stars.

Finally, we note that the triaxial configurations could also be invoked to explain the spin-up limit for rotating compact stars, which is far smaller than the mass-shedding limit. The results presented here and in Ref. [37] suggest that when triaxial deformations are taken into account, the rotational period of a compact star actually decreases as it gains angular momentum, e.g., by accretion, along the triaxial sequence. As a result, the "spin-up" process provided by the accretion of matter onto the pulsar can actually spin down the pulsar if the bifurcation point is reached. In this case, no accreting pulsar could spin up faster than the period at the bifurcation point. Of course, depending on the microphysical properties of the QS (e.g., the magnitude of the shear viscosity or of the breaking strain in the crust), it is also possible that other mechanisms of emission of gravitational waves (e.g., other dynamical instabilities such as the bar-mode instability [24,27] or the r-mode instability [90–92], or nonzero ellipticities) could intervene at lower spinning frequencies and therefore before the onset of instability to a triaxial deformation is reached [6,33]. As a result, the search for fast spinning pulsars with more powerful radio telescopes, such as the Square Kilometre Array (SKA) and the Five-Hundred-Meter Aperture Spherical Radio Telescope (FAST) [93,94], could provide important clues about the properties of pulsars and test the validity of the solid QS assumption [77].

ACKNOWLEDGMENTS

It is a pleasure to thank J. G. Lu, J. Papenfort, Z. Younsi, and all the members of the Pulsar group in Peking University and the Relastro group in Frankfurt for useful discussions. We will thank Dr. L. Shao and Dr. Y. Hu for their help with GW experiments. E. Z. is grateful to the China Scholarship Council for supporting the joint Ph.D. training in Frankfurt. This research is supported in part by the ERC synergy grant BlackHoleCam: Imaging the Event Horizon of Black Holes (Grant No. 610058), by NewCompStar, COST Action MP1304, by the LOEWE-Program in the Helmholtz International Center (HIC) for FAIR, by the European Union's Horizon 2020 Research and Innovation Programme (Grant No. 671698) (call FETHPC-1-2014, project ExaHyPE). This work is supported by the National Key R&D Program (Grant No. 2017YFA0402600) and NNSF (Grants No. 11673002 and No. U1531243). A. T. is supported by NSF Grants No. PHY-1662211 and No. PHY-1602536, and NASA Grant No. 80NSSC17K0070. K. U. is supported by JSPS Grant-in-Aid for Scientific Research(C) No. 15K05085.

[1] B. P. Abbot *et al.* (LIGO Scientific Collaboration and Virgo Collaboration), Phys. Rev. Lett. **119**, 161101 (2017).
[2] B. P. Abbott *et al.* (LIGO Scientific Collaboration and Virgo Collaboration), Astrophys. J. Lett. **848**, L12 (2017).
[3] B. P. Abbot *et al.* (LIGO Scientific Collaboration, Virgo Collaboration, F. Gamma-Ray Burst Monitor, and INTEGRAL), Astrophys. J. Lett. **848**, L13 (2017).
[4] B. P. Abbott *et al.* (LIGO Scientific Collaboration and Virgo Collaboration), Astrophys. J. **850**, L39 (2017).
[5] L. Baiotti and L. Rezzolla, Rep. Prog. Phys. **80**, 096901 (2017).
[6] N. Andersson, V. Ferrari, D. I. Jones, K. D. Kokkotas, B. Krishnan, J. S. Read, L. Rezzolla, and B. Zink, Gen. Relativ. Gravit. **43**, 409 (2011).

[7] A. A. Abramovici, W. Althouse, R. P. Drever, Y. Gursel, S. Kawamura, F. Raab, D. Shoemaker, L. Sievers, R. Spero, K. S. Thorne, R. Vogt, R. Weiss, S. Whitcomb, and M. Zuker, Science **256**, 325 (1992).
[8] M. Punturo *et al.*, Classical Quantum Gravity **27**, 084007 (2010).
[9] T. Accadia *et al.*, Classical Quantum Gravity **28**, 114002 (2011).
[10] K. Kuroda (LCGT Collaboration), Classical Quantum Gravity **27**, 084004 (2010).
[11] Y. Aso, Y. Michimura, K. Somiya, M. Ando, O. Miyakawa, T. Sekiguchi, D. Tatsumi, and H. Yamamoto, Phys. Rev. D **88**, 043007 (2013).
[12] S. Chandrasekhar, *The Silliman Foundation Lectures* (Yale University Press, New Haven, 1969).
[13] R. Meinel, M. Ansorg, A. Kleinwächter, G. Neugebauer, and D. Petroff, *Relativistic Figures of Equilibrium* (Cambridge University Press, Cambridge, England, 2008).
[14] J. L. Friedman and N. Stergioulas, *Rotating Relativistic Stars* (Cambridge University Press, Cambridge, UK, 2013).
[15] S. L. Shapiro and S. Zane, Astrophys. J. Suppl. Ser. **117**, 531 (1998).
[16] S. Bonazzola, J. Frieben, and E. Gourgoulhon, Astrophys. J. **460**, 379 (1996).
[17] D. Gondek-Rosińska and E. Gourgoulhon, Phys. Rev. D **66**, 044021 (2002).
[18] S. Bonazzola, J. Frieben, and E. Gourgoulhon, Astron. Astrophys. **331**, 280 (1998).
[19] J. L. Houser and J. M. Centrella, Phys. Rev. D **54**, 7278 (1996).
[20] B. K. Pickett, R. H. Durisen, and G. A. Davis, Astrophys. J. **458**, 714 (1996).
[21] J. D. Brown, Phys. Rev. D **62**, 084024 (2000).
[22] K. C. B. New, J. M. Centrella, and J. E. Tohline, Phys. Rev. D **62**, 064019 (2000).
[23] Y. T. Liu, Phys. Rev. D **65**, 124003 (2002).
[24] A. L. Watts, N. Andersson, and D. I. Jones, Astrophys. J. **618**, L37 (2005).
[25] L. Baiotti, R. De Pietri, G. M. Manca, and L. Rezzolla, Phys. Rev. D **75**, 044023 (2007).
[26] G. M. Manca, L. Baiotti, R. De Pietri, and L. Rezzolla, Classical Quantum Gravity **24**, S171 (2007).
[27] G. Corvino, L. Rezzolla, S. Bernuzzi, R. De Pietri, and B. Giacomazzo, Classical Quantum Gravity **27**, 114104 (2010).
[28] K. D. Camarda, P. Anninos, P. C. Fragile, and J. A. Font, Astrophys. J. **707**, 1610 (2009).
[29] L. Franci, R. De Pietri, K. Dionysopoulou, and L. Rezzolla, J. Phys. Conf. Ser. **470**, 012008 (2013).
[30] C. D. Muhlberger, F. H. Nouri, M. D. Duez, F. Foucart, L. E. Kidder, C. D. Ott, M. A. Scheel, B. Szilágyi, and S. A. Teukolsky, Phys. Rev. D **90**, 104014 (2014).
[31] N. Andersson, Classical Quantum Gravity **20**, R105 (2003).
[32] D. Lai and S. L. Shapiro, Astrophys. J. **442**, 259 (1995).
[33] L. Bildsten, Astrophys. J. Lett. **501**, L89 (1998).
[34] S. Woosley and T. Janka, Nat. Phys. **1**, 147 (2005).
[35] A. L. Watts, B. Krishnan, L. Bildsten, and B. F. Schutz, Mon. Not. R. Astron. Soc. **389**, 839 (2008).
[36] A. L. Piro and E. Thrane, Astrophys. J. **761**, 63 (2012).
[37] X. Huang, C. Markakis, N. Sugiyama, and K. Uryū, Phys. Rev. D **78**, 124023 (2008).
[38] K. Uryū, A. Tsokaros, F. Galeazzi, H. Hotta, M. Sugimura, K. Taniguchi, and S. Yoshida, Phys. Rev. D **93**, 044056 (2016).
[39] R. A. James, Astrophys. J. **140**, 552 (1964).
[40] I. Hachisu and Y. Eriguchi, Prog. Theor. Phys. **68**, 206 (1982).
[41] D. Lai, F. A. Rasio, and S. L. Shapiro, Astrophys. J. Suppl. Ser. **88**, 205 (1993).
[42] A. R. Bodmer, Phys. Rev. D **4**, 1601 (1971).
[43] E. Witten, Phys. Rev. D **30**, 272 (1984).
[44] Z. G. Dai, S. Q. Wang, J. S. Wang, L. J. Wang, and Y. W. Yu, Astrophys. J. **817**, 132 (2016).
[45] X. Y. Lai, Y. W. Yu, E. P. Zhou, Y. Y. Li, and R. X. Xu, arXiv:1710.04964.
[46] A. Li, B. Zhang, N.-B. Zhang, H. Gao, B. Qi, and T. Liu, Phys. Rev. D **94**, 083010 (2016).
[47] N. Itoh, Prog. Theor. Phys. **44**, 291 (1970).
[48] C. Alcock, E. Farhi, and A. Olinto, Astrophys. J. **310**, 261 (1986).
[49] P. Haensel, J. L. Zdunik, and R. Schaefer, Astron. Astrophys. **160**, 121 (1986).
[50] D. Gondek-Rosińska, T. Bulik, L. Zdunik, E. Gourgoulhon, S. Ray, J. Dey, and M. Dey, Astron. Astrophys. **363**, 1005 (2000).
[51] E. Gourgoulhon, P. Haensel, R. Livine, E. Paluch, S. Bonazzola, and J.-A. Marck, Astron. Astrophys. **349**, 851 (1999).
[52] N. Stergioulas, W. Kluźniak, and T. Bulik, Astron. Astrophys. **352**, L116 (1999).
[53] M. Szkudlarek, D. Gondek-Rosińska, L. Villain, and M. Ansorg, in *Electromagnetic Radiation from Pulsars and Magnetars*, Astronomical Society of the Pacific Conference Series, Vol. 466, edited by W. Lewandowski, O. Maron, and J. Kijak (2012), p. 231.
[54] D. Gondek-Rosinska, P. Haensel, J. L. Zdunik, and E. Gourgoulhon, in *IAU Colloq. 177: Pulsar Astronomy—2000 and Beyond*, Astronomical Society of the Pacific Conference Series, Vol. 202, edited by M. Kramer, N. Wex, and R. Wielebinski (2000), p. 661.
[55] D. Gondek-Rosińska, N. Stergioulas, T. Bulik, W. Kluźniak, and E. Gourgoulhon, Astron. Astrophys. **380**, 190 (2001).
[56] D. Gondek-Rosińska, E. Gourgoulhon, and P. Haensel, Astron. Astrophys. **412**, 777 (2003).
[57] K. Uryū and A. Tsokaros, Phys. Rev. D **85**, 064014 (2012).
[58] K. Uryū, A. Tsokaros, and P. Grandclement, Phys. Rev. D **86**, 104001 (2012).
[59] A. Tsokaros and K. Uryū, J. Eng. Math. **82**, 133 (2013).
[60] A. Tsokaros, K. Uryū, and L. Rezzolla, Phys. Rev. D **91**, 104030 (2015).
[61] A. Tsokaros, M. Ruiz, V. Paschalidis, S. L. Shapiro, L. Baiotti, and K. Uryū, Phys. Rev. D **95**, 124057 (2017).
[62] L. Rezzolla and O. Zanotti, *Relativistic Hydrodynamics* (Oxford University Press, Oxford, UK, 2013).
[63] J. Isenberg and J. Nester, in *General Relativity and Gravitation, One Hundred Years after the Birth of Albert*

Einstein, edited by A. Held (Plenum Press, New York, 1980), Vol. 1, p. 23.
[64] J. A. Isenberg, Int. J. Mod. Phys. **D17**, 265 (2008).
[65] J. R. Wilson and G. J. Mathews, in *Frontiers in Numerical Relativity*, edited by C. R. Evans, L. S. Finn, and D. W. Hobill (1989), pp. 306–314.
[66] A. Chodos, R. L. Jaffe, K. Johnson, C. B. Thorn, and V. F. Weisskopf, Phys. Rev. D **9**, 3471 (1974).
[67] F. Limousin, D. Gondek-Rosińska, and E. Gourgoulhon, Phys. Rev. D **71**, 064012 (2005).
[68] X. Y. Lai and R. X. Xu, Mon. Not. R. Astron. Soc. **398**, L31 (2009).
[69] X. Y. Lai and R. X. Xu, J. Phys. Conf. Ser. **861**, 012027 (2017).
[70] Y.-J. Guo, X.-Y. Lai, and R.-X. Xu, Chin. Phys. C **38**, 055101 (2014).
[71] X.-Y. Lai and R.-X. Xu, Res. Astron. Astrophys. **11**, 687 (2011).
[72] P. B. Demorest, T. Pennucci, S. M. Ransom, M. S. E. Roberts, and J. W. T. Hessels, Nature (London) **467**, 1081 (2010).
[73] J. Antoniadis *et al.*, Science **340**, 1233232 (2013).
[74] E. P. Zhou, J. G. Lu, H. Tong, and R. X. Xu, Mon. Not. R. Astron. Soc. **443**, 2705 (2014).
[75] R. Xu and E. Liang, Sci. China Ser. G-Phys. Mech. Astron. **52**, 315 (2009).
[76] W. Wang, J. Lu, H. Tong, M. Ge, Z. Li, Y. Men, and R. Xu, Astrophys. J. **837**, 81 (2017).
[77] R. X. Xu, Astrophys. J. Lett. **596**, L59 (2003).
[78] J. S. Read, B. D. Lackey, B. J. Owen, and J. L. Friedman, Phys. Rev. D **79**, 124032 (2009).
[79] A. Li, Z.-Y. Zhu, and X. Zhou, Astrophys. J. **844**, 41 (2017).
[80] S. Bhattacharyya, I. Bombaci, D. Logoteta, and A. V. Thampan, Mon. Not. R. Astron. Soc. **457**, 3101 (2016).
[81] M. Alford, M. Braby, M. Paris, and S. Reddy, Astrophys. J. **629**, 969 (2005).
[82] G. Baym, T. Hatsuda, T. Kojo, P. D. Powell, Y. Song, and T. Takatsuka, arXiv:1707.04966.
[83] J. P. Ostriker and J. W.-K. Mark, Astrophys. J. **151**, 1075 (1968).
[84] H. Komatsu, Y. Eriguchi, and I. Hachisu, Mon. Not. R. Astron. Soc. **237**, 355 (1989).
[85] A. Tsokaros, B. C. Mundim, F. Galeazzi, L. Rezzolla, and K. Uryū, Phys. Rev. D **94**, 044049 (2016).
[86] A. Tsokaros and K. Uryū, Phys. Rev. D **75**, 044026 (2007).
[87] L. R. Weih, E. R. Most, and L. Rezzolla, Mon. Not. R. Astron. Soc. **473**, L126 (2018).
[88] C. Breu and L. Rezzolla, Mon. Not. R. Astron. Soc. **459**, 646 (2016).
[89] K. Uryū, A. Tsokaros, L. Baiotti, F. Galeazzi, N. Sugiyama, K. Taniguchi, and S. Yoshida, Phys. Rev. D **94**, 101302 (2016).
[90] N. Andersson, Astrophys. J. **502**, 708 (1998).
[91] J. L. Friedman and S. M. Morsink, Astrophys. J. **502**, 714 (1998).
[92] N. Andersson, K. D. Kokkotas, and N. Stergioulas, Astrophys. J. **516**, 307 (1999).
[93] M. Kramer and B. Stappers, arXiv:1507.04423.
[94] R. Nan, D. Li, C. Jin, Q. Wang, L. Zhu, W. Zhu, H. Zhang, Y. Yue, and L. Qian, Int. J. Mod. Phys. D **D20**, 989 (2011).